Design, Control, and Experimental Evaluation of a Novel Robotic Glove System for Patients With Brachial Plexus Injuries

Wenda Xu, Yunfei Guo, Cesar Bravo, and Pinhas Ben-Tzvi, *Senior Member, IEEE*

***Abstract*—This article presents the development of an exoskeleton glove system for people who suffer from brachial plexus injuries, aiming to assist their lost grasping functionality. The robotic system consists of a portable glove system and an embedded controller. The glove system consists of linear series elastic actuators, rotary series elastic actuators, and optimized finger linkages to provide imitated human motion to each finger and a coupled motion of the hand. The design principles and optimization strategies were investigated to balance functionality, portability, and stability. The model-based force control strategy compensated with a backlash model and model-free force control strategy are presented and compared. Results show that our proposed model-free control method achieves the goal of accurate force control. Finally, experiments were conducted with the prototype of the developed integrated exoskeleton glove system. Results from three subjects with 150 trials show that our proposed exoskeleton glove system has the potential to be used as a rehabilitation device for patients.**

***Index Terms*—Exoskeleton glove, grasp assistance, series elastic actuator (SEA), wearable robotics.**

I. Introduction

APPROXIMATELY 19.9 million people in the United States suffer from upper body impairments that affect their ability to lift or grasp objects [1]. Of those people, 6.7 million experience difficulties in grasping everyday objects, such as a cup or a pencil, leading to difficulties in performing activities of daily living (ADLs). Brachial plexus injury (BPI), which is mostly caused by motor vehicle accidents and extreme sporting accidents [2], is one of the most devastating injuries from the patients' point of view [3]. It is a severe peripheral nerve injury affecting the upper extremities causing functional damage and physical disability [3]. Individuals who suffer from BPI can experience loss of muscle control and feeling in their shoulder, arm, and hand. Previous studies [4] have proven that surgical options can successfully restore shoulder and arm function but are less effective in returning sensation and mobility to the hand due to the distance between the working nerves in the zone of injury and the targeted zone of rehabilitation. In such situations, robotic exoskeletons can provide a promising way to help patients regain the lost function in their hands.

In recent years, several hand rehabilitation exoskeletons have been developed, which include about 46 daily assistance devices [5]. Compared with the traditional stationary devices [6], [7], wearable devices attract more attention due to their portability. As an exoskeleton device for ADLs, three major design requirements need to be satisfied [8]: compactness, simplicity of the mechanism, and good ergonomics. Soft robotic gloves [9], [10], [11], [12] can achieve a simple design with good wearability provided by compliant materials. However, these design innovations cannot avoid using thick inflatable segments over the fingers in order to induce bending. In addition, the need to use air compressors for operation limits the glove's portability [13]. Other devices driven by hydraulic or pneumatic actuators suffer from similar challenges. Cable-driven and Bowden-driven gloves [14], [15], [16] have the advantage of compact size and remote motor installation. However, tendon transmissions can suffer from cable breakage and sometimes require complex routing. Additionally, to achieve bidirectional actuation, another actuator is often required in order to apply force in the opposite direction. The direct linkage transmission gloves [17], [18], [19], [20], [21] provide a simple mechanism that can be readily designed to accommodate ergonomic requirements. However, many of them have large weight or bulky design, which causes discomfort to patients.

Besides the hardware design, the control strategy is also a challenge for wearable rehabilitation devices. Previously, researchers have proven that force control based strategies are more efficient for upper limb rehabilitation devices [22], [23], [24] than position-based control strategies [25]. Traditional

Manuscript received 19 March 2022; revised 12 September 2022; accepted 17 October 2022. Date of publication 23 November 2022; date of current version 5 April 2023. This work was supported by the Eunice Kennedy Shriver National Institute of Child Health & Human Development of the National Institutes of Health under Award R21HD095027. The content is solely the responsibility of the authors and does not necessarily represent the official views of the National Institutes of Health. This paper was recommended for publication by Associate Editor F. Ficuciello and Editor E. Yoshida upon evaluation of the reviewers' comments. *(Corresponding author: Pinhas Ben-Tzvi.)*

This work involved human subjects or animals in its research. Approval of all ethical and experimental procedures and protocols was granted by Carilion Clinic Institutional Review Board under Application No. IRB-19-330.

Wenda Xu is with the Mechanical Engineering Department, Virginia Tech, Blacksburg, VA 24061 USA (e-mail: wenda@vt.edu).

Yunfei Guo is with the Electrical and Computer Engineering Department, Virginia Tech, Blacksburg, VA 24061 USA (e-mail: yunfei96@vt.edu).

Cesar Bravo is with the Carilion Clinic Institute of Orthopaedics and Neurosciences, Virginia Tech Carilion School of Medicine, Roanoke, VA 24014 USA (e-mail: cjbravo@carilionclinic.org).

Pinhas Ben-Tzvi is with the Mechanical Engineering and Electrical and Computer Engineering Departments, Virginia Tech, Blacksburg, VA 24061 USA (e-mail: bentzvi@vt.edu).

This article has supplementary material provided by the authors and color versions of one or more figures available at https://doi.org/10.1109/TRO.2022.3220973.

Digital Object Identifier 10.1109/TRO.2022.3220973

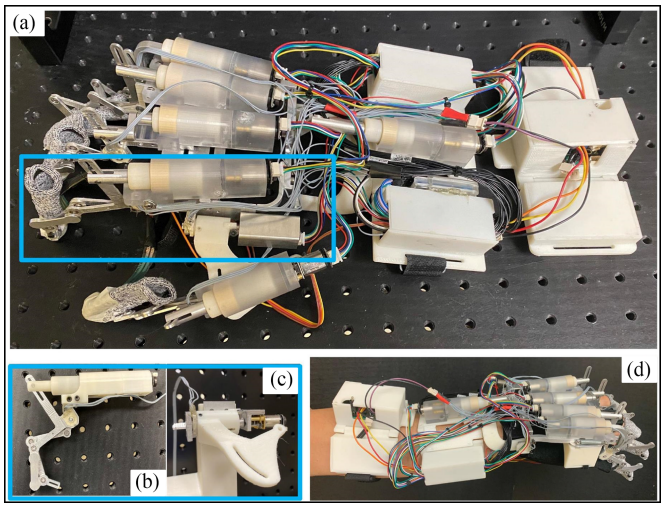

Fig. 1. (a) Overview of the exoskeleton glove system, (b) index finger linear series elastic actuators (SEA), (c) rotary SEA, (d) user wearing the exoskeleton glove. Blue: enlarged view of index finger linear SEA and rotary SEA.

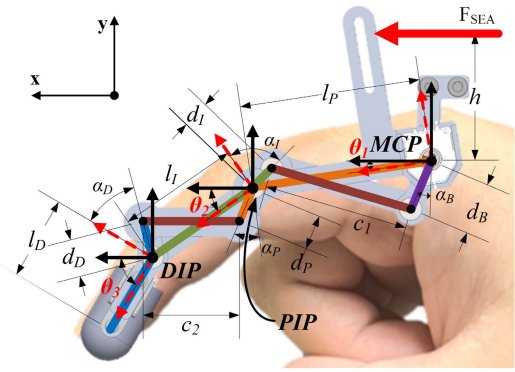

Fig. 2. Mechanism schematic and kinematic model of the index exoskeleton finger linkage. Different colors represent different links: blue link—distal phalanx; green link—intermediate phalanx; orange link—proximal phalanx; brown links—constraint links.

model-based force control requires an accurate dynamic model to consider various conditions. However, it is difficult to build an ideal model since many factors, such as backlash, collisions, friction force, and deformation, are difficult to model and measure. In contrast, a simplified model would be easier to build but may ignore important variables resulting in low accuracy.

Given the challenges of previous wearable devices and control strategies, we propose a new exoskeleton glove system that is compact, relatively simple, multifunctional, and user-friendly for grasping based on an accurate model-free force control. This article presents the design details, optimization, control, and development of the proposed exoskeleton glove system (Fig. 1). The glove is driven by two types of evolutionary SEAs compared with the previous design [26]. The linkage system couples the motion of the metacarpophalangeal (MCP), proximal interphalangeal (PIP), and distal interphalangeal (DIP) joints into one degree of freedom to greatly simplify the mechanism. It is optimized based on ergonomic factors to provide a comfortable wearing experience for patients and also make up for design deficiencies based on lessons learned from previous research [27]. Besides the basic bending mechanism of each finger, a passive abduction–adduction mechanism has also been implemented. The model-free data-driven force control strategy is presented and compared against a model-based backlash-compensated force control strategy to achieve a balance between the computation time and accuracy. Finally, a prototype of the proposed exoskeleton glove system with integrated object slip detection [28] and voice activation [29], [30] was developed.

The unique characteristics of the proposed exoskeleton glove system can be summarized as follows: 1) an integrated system that contains a linkage mechanism that satisfies ergonomics and includes a human–machine interface through voice activation; 2) the exoskeleton glove system was designed to fit over the entire hand; and 3) the glove system is implemented with accurate force control, which provides the feasibility for intelligent control. These, along with other improvements implemented based on previous research [26], [31], [32], make our proposed glove system portable, lightweight, and much more capable than before.

The remainder of the article is organized as follows. In Section II, the design and optimization of the glove system are introduced including two types of SEAs, linkages, and the full glove. In Section III, the design of electronics is introduced. In Section IV, the backlash mathematical model and the two types of force control strategies are presented. In Section V, experiments with the control strategies and prototype of the entire exoskeleton glove system are performed to verify the functionality of the system. Lastly, Section VI concludes the article.

II. Design

In this section, we provide details on the design principles of the finger mechanism, motion trajectory optimizations for each finger, and the design of both the linear series elastic actuator (LSEA) and the rotary series elastic actuator (RSEA). The final configurations of the prototype are introduced for implementation. The total weight of the whole glove system (including electronics and batteries) is 759 g.

A. Exoskeleton Finger Mechanism Design

The goal of the exoskeleton finger mechanism design is to build a compact finger linkage that can imitate the human finger grasping motion while maximizing the workspace of each finger. Each human finger consists of three different joints, including the MCP joint, the PIP joint, and the DIP joint (shown in Fig. 2). The DIP and PIP joints have one flexion-extension DOF, but the MCP joint has one more abduction–adduction DOF. The thumb digit consists of interphalangeal (IP), MCP, and carpometacarpal (CMC) joints. Similarly, the IP and MCP joints have one DOF (flexion–extension), but the CMC has two DOFs, including flexion–extension and abduction–adduction [33].

Previous research [34], [35], [36] has proven that a finger linkage with reduced DOFs can achieve most of the grasping

motions needed for ADLs because of the coupled motion of different joints on each finger while grasping. Furthermore, an exoskeleton finger linkage with reduced DOFs requires fewer actuators for grasping, which results in a more compact design. To overcome the problems mentioned in Section I and achieve the design goals proposed above, we adopted the coupling mechanism and attached it to the side of each finger. This allows the entire exoskeleton to be more slim and more lightweight with respect to the existing design. Fig. 2 shows an example of the proposed mechanism. The joints of each exoskeleton finger mechanism are coincident with the joints of the human finger. It is worth mentioning that the MCP joint of the middle and ring fingers on the exoskeleton are placed forward of the human counterparts to avoid interference with the finger-webs. The blue, green, and orange links shown in Fig. 2 represent the distal phalanx, intermediate phalanx, and proximal phalanx, respectively. The adjacent links are connected at their extensions by constraint links (brown links) for coupling the motion. Therefore, the three DOFs for the flexion–extension motion are reduced to one DOF flexion–extension motion for each finger. The rotations of the first two joints on the thumb are coupled by the same method.

The abduction–adduction motion is also important for stable and comfortable grasping [37]. The web between fingers and the interossei muscles help to perform the adduction motion during the process of closing the hand. The proposed exoskeleton glove implements a passive abduction–adduction mechanism as shown in Fig. 3. A revolute joint is added at the bottom of the SEA to connect the base and the housing (partial view in Fig. 3). A soft spring on the side is used to connect the housing of the SEA and the base for abduction motion while opening the hand. A mechanical limit is added to restrict the maximum angle and prevent over-rotation. When the patient's hand opens, the spring will pull the finger to one side until it reaches the mechanical limit to achieve abduction motion and hold the position. When the patient's hand closes, the internal mechanism of the human finger mentioned above will force the hand to perform the adduction motion.

For most ADLs, the weight of the goal object is unknown. Therefore, predefining a specific grasp force for each object is unrealistic. Thus, it is necessary to integrate a slip detection function. Previous research works [30], [38] have shown that sensor fusion can help with slip detection. This method is implemented by attaching force-sensing resistor (FSR) sensors on the fingertip of the thumb and index finger of the exoskeleton. The control logic used in our exoskeleton is based on a slip–grasp policy. Upon receiving a voice command, the SEAs will first apply a predefined force to ensure the exoskeleton made contact with the object. We used FSRs to verify that the object has contact with either index or thumb finger. The slip detection is activated after the initial force has been applied. We monitored the change in force in both FSR and SEA readings. If either FSRs or SEAs measured a drop in force for more than 5%, 1 N force will be added incrementally to all fingers. The FSR sensors only work for contact detection and slip detection but not for force measurement due to their high sensitivity and low linearity.

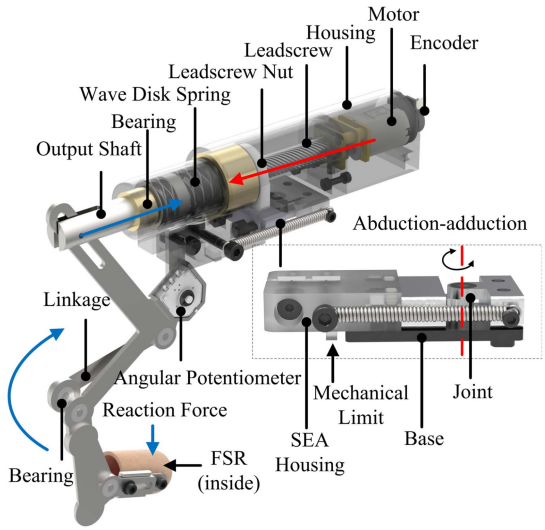

Fig. 3. Perspective view of the index linkage. The screw nut guided by leadscrew connects to the output shaft. The compressed wave disk spring between the output shaft and screw nut measures the force by its deformation when the fingertip makes contact with an object. The red arrow shows the force generation flow and the blue arrow shows the force measurement flow. The distal link is adjustable and can be extended by 7 mm. The LSEA can slide on the base to accommodate different hand sizes. The partial view shows the details of the abduction–adduction mechanism. It is implemented at the bottom of the SEA to connect the finger linkage with the base through a joint. At the initial position, the hand needs to be open and be ready for grasping. The spring on the side pulls the exoskeleton finger linkage to the side to perform the abduction. Mechanical limits were added to avoid excess force to the fingers. The palmar interossei muscle group will perform the adduction automatically and stretch the spring while grasping.

B. Kinematics Model and Optimization of the Exoskeleton Finger

In order to optimize the finger mechanism design presented in Section II-A, the kinematics of the mechanism needs to be modeled. The kinematic model used in previous research [27] did not consider the trajectory limitation of the human hand. In this research, the index exoskeleton finger linkage is selected for illustration purposes. Assuming that the origin of the global coordinate frame is located at the MCP joint as shown in Fig. 2, the open-loop equation for the kinematic chain of the finger exoskeleton linkage is given by

$$l_P e^{\theta_1 i} + l_I e^{\theta_2 i} + l_D e^{\theta_3 i} = x_{\text{tip}} + y_{\text{tip}} i \tag{1}$$

where l_1, l_2, and l_3 are the lengths of the proximal link, intermediate link, and distal link of the exoskeleton, respectively. θ_1, θ_2, and θ_3 are the angles between the corresponding link and the x-axis. (x_{tip}, y_{tip}) represents the fingertip coordinate in the global frame of reference.

Forward kinematics are used for evaluating the angles θ_1, θ_2, and θ_3. The relationship between them is formed by adding constraint links to couple their motion. The constraints can be expressed as follows:

$$\begin{aligned} c_1^2 = {} & [l_P \cos\theta_1 - d_I \sin(\alpha_I - \theta_2) - d_B \sin\alpha_B]^2 \\ & + [l_P \sin\theta_1 - d_I \cos(\alpha_I - \theta_2) - d_B \cos\alpha_B]^2 \end{aligned} \tag{2}$$

$$c_2^2 = [l_I \cos\theta_2 + d_D \sin(\theta_3 - \alpha_D) - d_P \sin(\alpha_P - \theta_1)]^2 + [l_I \sin\theta_2 - d_D \cos(\theta_3 - \alpha_D) - d_P \cos(\alpha_P - \theta_1)]^2 \tag{3}$$

where c_1 and c_2 are the lengths of the corresponding constraint links. d_B, d_P, d_I, and d_D are the extension lengths of the base, proximal link, intermediate link, and distal link to be connected with the constraint links, respectively. α_B, α_P, α_I, and α_D are the angles of extension of the base, proximal link, intermediate link, and distal link with respect to the y-axis of the local coordinates (only acute angles), respectively.

Because θ_1 is driven by the actuator directly, given a particular θ_1, the unique corresponding θ_2 and θ_3 can be derived based on the above constraint equations. Analytically, θ_2 and θ_3 can be expressed as follows:

$$\theta_2 = -\tan^{-1}\left\{\frac{\sqrt{-[A+(c_1-d_I)^2][A+(c_1+d_I)^2]}}{-c_1^2 - A + B + d_I^2} - \frac{2d_I l_P \cos\theta_1 - 2d_B d_I \sin\alpha_B}{-c_1^2 - A + B + d_I^2}\right\} + \alpha_I \tag{4}$$

where $A = 2d_B l_P \sin(\alpha_B + \theta_1) - l_P^2 - d_B^2$ and $B = 2d_I l_D \sin\theta_1 - 2d_B d_I \cos\alpha_B$.

$$\theta_3 = \tan^{-1}\left\{\frac{\sqrt{-[C+(c_2-d_D)^2][C+(c_2+d_D)^2]}}{-c_2^2 - C + D + d_D^2} - \frac{2d_D l_I \cos\theta_2 - 2d_P d_D \sin(\alpha_P - \theta_1)}{-c_2^2 - C + D + d_D^2}\right\} + \alpha_D \tag{5}$$

where $C = 2d_P l_I \sin(\alpha_P - \theta_1 + \theta_2) - l_I^2 - d_P^2$ and $D = -2d_D d_P \cos(\alpha_P - \theta_1) + 2d_D l_I \sin\theta_2$.

The Jacobian of the mechanism is calculated to evaluate the velocity kinematics. Numerical computation in MATLAB is used to evaluate the Jacobian of the system. The velocity of the endpoints of the exoskeleton linkages in the global x and y directions can be expressed as follows:

$$[\dot{\mathbf{p}}]_{2\times1} = [\mathbf{J}]_{2\times1}[\dot{\boldsymbol{\theta}}_1]_{1\times1}. \tag{6}$$

The geometric parameters of each link, especially the joints' position and the length of the constraint links, determine the properties of the linkage such as workspace and force transmission ratio. The optimization process is used to find the values for the design variables that minimize the objective function, which are related to the properties of the linkage, while satisfying the constraints. Considering the passive abduction–adduction mechanism, each exoskeleton finger mechanism is optimized in 2-D space separately.

Based on the analysis of the kinematics model, all of the parameters, except for l_P, l_I, l_D, and θ_1, are design variables for each specific exoskeleton finger. To build a more general exoskeleton glove that is suitable for most people, the values of l_P, l_I, and l_D for each linkage are determined by considering the results of the previous research [39], which provides the range of length of the finger phalanges, and the measurement results of the user's hand. The final selected values are shown in Table I. To be better able to imitate a human hand's grasp motion, the optimization takes the coincidence of the fingertips, the PIP joint positions, and the DIP joint positions into account. The rotation angles of each joint on the grasping trajectory are obtained from the HUST dataset [40]. The dataset provides broadly 33 types of grasps with respect to 30 subjects. The data from Grasp 2 of Subject 24, which performs a small diameter grasp, is selected as a reference trajectory due to its large bending angles. Four points, which are equally distributed on the reference trajectory, are selected as reference points. It is worth mentioning that θ_1 is selected by mapping rotation angles of the MCP joint into $0°$–$40°$ because of the rotation limitation of each exoskeleton finger mechanism. The objective function Z is the sum of the distance between endpoints, the distance between DIP joints, and the distance between PIP joints on four reference points with different weights. It can be expressed as follows:

TABLE I
LINKS LENGTH OF EACH FINGER

Finger name	l_P (mm)	l_I (mm)	l_D (mm)
Index	42	25	17.7
Middle	47	28.3	17.4
Ring	43	26.2	17.3
Little	31.3	20.5	16
Thumb	32	–	22

$$Z = \sum_{i=1}^{3} \mathbf{w}_i^T \mathbf{e}_i \tag{7}$$

where $[\mathbf{w_1}]_{4\times1}$ represents the weights of endpoints with respect to each reference point, $[\mathbf{w_2}]_{4\times1}$ represents the weights of the DIP joints with respect to each reference point, $[\mathbf{w_3}]_{4\times1}$ represents the weights of the PIP joints with respect to each reference point, $[\mathbf{e_1}]_{4\times1}$ represents the distances of endpoints with respect to each reference point, $[\mathbf{e_2}]_{4\times1}$ represents the distances of the DIP joints with respect to each reference point, and $[\mathbf{e_3}]_{4\times1}$ represents the distances of the PIP joints with respect to each reference point. Fig. 4 shows the index finger joints trajectory with different values of the MCP rotation angle. The angle varies from $5°$ to $35°$ and leaves $5°$ to reach the limitation for safety.

Considering the need to avoid interference between the finger-webs and the finger linkages, the exoskeleton MCP joints for the ring and middle fingers were offset forward and upward with respect to the corresponding finger's MCP joint. The offset of the MCP joint between the exoskeleton and the human finger are also design variables to be optimized with inequality constraints. The trajectory for a small-diameter cylindrical grasp with the optimized exoskeleton glove is shown in Fig. 5.

To have a better grasp performance, we also considered the impact of the coupled wrist motion since the hand impairments also result in the wrist impairments. An LSEA is used to connect the wrist and the glove to help patients hold the initial position of the hand for grasping. The LSEA on the wrist will be automatically adjusted to maintain the initial position smoothly. It is worth mentioning that we only considered the flexion and extension since these movements are commonly used for our selected grasp types mentioned in Section V.

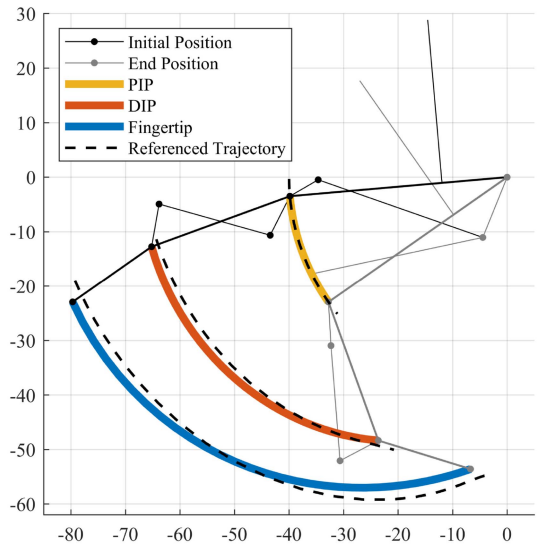

Fig. 4. Kinematic simulation of the optimized index finger exoskeleton rotating around the MCP joint from 5° to 35°. The trajectories of the PIP joint, DIP joint, and fingertip are shown. The referenced trajectories, which are based on the referenced joint angle with a selected finger length, are also shown for comparison.

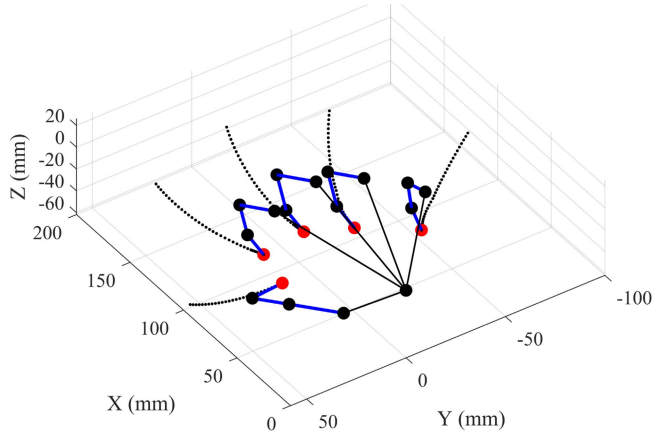

Fig. 5. Simulation of a small diameter cylindrical grasp with optimized finger linkages. The blue bars represent the exoskeleton links. The black dots represent the exoskeleton joints. The red dots represent the endpoints of each linkage. The dotted lines represent the trajectories of the fingers' motion.

C. Series Elastic Actuation

To achieve accurate and stable force control, comfortable wearability, and safe human–robot interaction, series elastic actuators (SEAs) [41] were incorporated into our proposed glove design. The SEAs do not only act as force actuators or force sensors but also as compliant elements to introduce pliability and to avoid injury to the user. Two types of SEAs were designed, including LSEA and RSEA. The LSEAs are used to provide and measure forces for the five fingers and wrist, while the RSEA is used to provide and measure torque for the thenar. The perspective view in Fig. 3 shows the components of the LSEA. The wave disk springs are used as elastic elements because of their lower operating height and their ability to transmit 100% of the axial load. It is worth mentioning that the leadscrew nut, two wave disk springs, and the output shaft are firmly connected and move as one slider on the leadscrew, powered by a motor mounted at the end. In this design, only the back spring works as the elastic element for the LSEA, and the front one works as a buffer to avoid harm from sudden force application. The output motor torque is transmitted to an output force through a gearbox, leadscrew, and wave disk spring. Considering the following leadscrew load-lifting calculation by

$$\tan(\lambda) = \frac{l}{\pi d_m} \tag{8}$$

$$F_{\text{raise}} = \frac{2T}{d_m}\eta_s \left(\frac{1 - \mu \sec\alpha \tan\lambda}{\mu \sec\alpha + \tan\lambda}\right) \tag{9}$$

the output force F_o and speed v_o at the SEA output shaft, related to the input torque T_m and speed n_m from the motor, can be calculated according to

$$F_o = \frac{2T_m i}{d_m}\left(\frac{1 - \mu \sec\alpha \tan\lambda}{\mu \sec\alpha + \tan\lambda}\right)\eta_s\eta_g\eta_m \tag{10}$$

$$v_o = \frac{l n_m}{60 i} \tag{11}$$

where l is the lead of the leadscrew; d_m is the pitch diameter; λ is the lead angle; α is the thread angle; μ is the friction coefficient; i is the reduction rate; η_s is the efficiency of the leadscrew; η_g is the transmission efficiency; and η_m is the efficiency of the motor combination. The transmission efficiency is defined as the ratio of the output force and the input force.

The above equations specify the largest force that can be generated by the LSEA. However, the measurable forces (F_{SEA}) are determined by the displacement of elastic elements. For the LSEA, it is hard to measure the displacement of elastic elements inside the LSEA directly. Thus, the displacement measurement (Δs) of the wave disk spring is performed by calculating the relationship between the readings from the potentiometer (θ, initial angle θ_i) on the linkage and the motor encoder (Δticks, compared with the initial position), as shown in the following equation:

$$F_{\text{SEA}} = k\Delta s = k\left[\frac{l\Delta\text{ticks}}{N_{\text{cpr}} i} - h(\tan\theta - \tan\theta_i)\right] \tag{12}$$

where k is the spring constant, h is the height from the LSEA output shaft to the MCP joint, and N_{cpr} is the counts per revolution of the encoder.

The operating principle of the RSEA (Fig. 6) is similar to the LSEA. However, the displacement of the wave disk spring is replaced by the angular deflection of a torsion spring. One leg of the torsion spring is connected to the inner shaft, which is powered by the motor directly, while the other one is connected to the thumb thenar part that is attached to the hand. When the patient performs a grasp, the difference of the rotation angle between the inner shaft and the thumb thenar is used to calculate the torque, which is applied to the thumb thenar as $\tau = \kappa\Delta\phi$, where τ is the generated torque, κ is the torsion constant, and $\Delta\phi$ is the angle difference between the inner shaft and the thumb thenar read by the angular potentiometer.

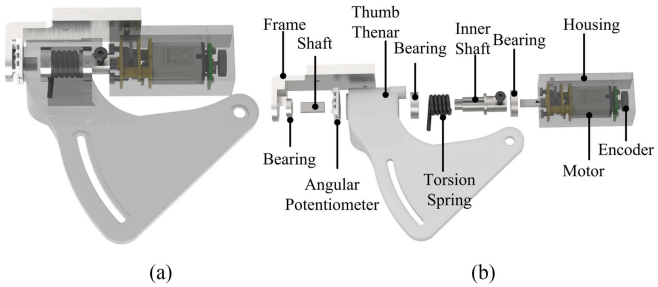

Fig. 6. Design of RSEA for thumb thenar: (a) perspective view of the RSEA; (b) exploded view of the RSEA.

According to the previous research [42], [43], the LSEA is designed to measure 10 N on each finger. The detailed fingertip force derivation is discussed in Section IV. To satisfy the measurement requirements and maintain the small size of the transmission system, the wave disk spring ($k = 5.5$ N·mm and load $= 40$ N), the dual shaft gear motors ($i = 380{:}1$, $T_m = 490$ N·mm, and $n_m = 32\,300$ r/min) and the leadscrew ($l = 20$ mm, $d_m = 5.5$ mm, $\alpha = 30°$, $\mu = 0.2$, $\eta_s = 0.78$, and $\lambda = 49.27°$) have been selected. For the RSEA, a more powerful dual shaft gear motors ($i = 1000{:}1$, $T_m = 980$ N·mm, and $n_m = 35000$ r/min) and a torsion spring ($\kappa = 1.85$ N·mm/°) were chosen.

III. Electrical Design

A. Sensors

Each SEA includes a Bourns 3382H angular potentiometer on the side of the linkage to measure the SEA output shaft position and a 12-b Pololu magnetic encoder to measure the input shaft position. A voltage of 21 V is applied to the potentiometer on the linkage to achieve better measurement accuracy at small angular displacements. Both mechanical limits and overvoltage protection circuits were implemented to ensure that the measured voltage is within a measurable range. Sparkfun SN-09375 (FSR) is mounted inside the finger sleeve to provide small force slip detection and contact detection due to its exponential force sensitivity but low linearity.

B. Electrical Components

The glove's onboard electronics consist of four main parts, including three separate PCBs, and a lithium-ion battery pack, as shown in Fig. 7. Each component is connected using quickly detachable connectors for easier repair and replacement. Three individual PCBs contain two control units to process the signal from sensors and control the motor. Control unit 1 integrates a Teensy 4.1 microcontroller for multithreading signal processing and force control, and an HC 5.0 Bluetooth (BT) model for wireless communication. This control unit is responsible for processing signals from the sensors, sending data to the server, receiving commands from the server, and performing force control. This control unit also has overvoltage protection circuit for safely reading potentiometer signals. Control unit 2 receives signals from control unit 1 and controls seven motors using Pololu md21a motor controller. The power supply PCB is used

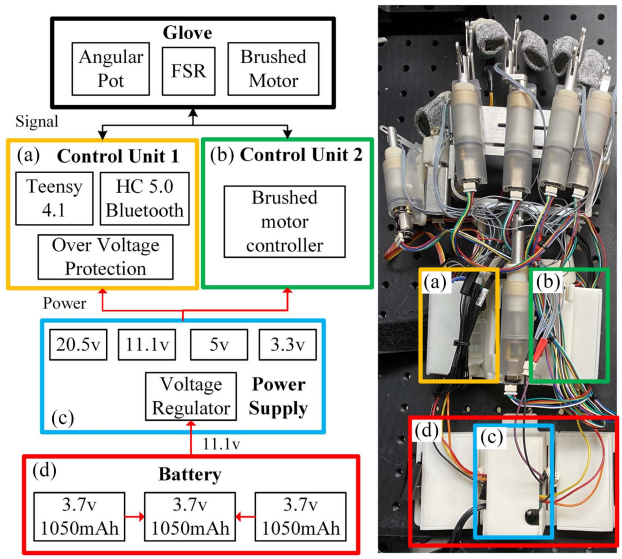

Fig. 7. Electronics design overview: (a) microcontroller board, (b) brushed motor controller board, (c) power conversion board, and (d) three-in-one battery package.

for power conversion to provide various voltages to different subsystems. The lithium-ion battery pack contains three DTP-603050 batteries (3.7 V 1050 mAh) in series to provide 11.1-V output with a 1-C discharge rate.

C. Power Consumption

The average power consumption (P) is measured by monitoring the instant current (I_{inst}) of an external power source when performing the grasping experiments above and calculated using the following equation:

$$P = \frac{U \cdot \sum I_{\text{inst}}}{t} \tag{13}$$

where U is the 11.1-V supplied voltage and t is the total time cost during the grasping.

The average power consumption for active grasping is 4.7 W, and 1.7 W for idle. A battery package that contains three 1050-mAh Li–Po batteries is used to power the device. The batteries can hold up to 2.5 h of continuous operation or 6.7 h of idling, which is sufficient for our application.

IV. Control

In this section, we provide the estimation method used to eliminate the impact of backlash and develop two types of prediction methods for LSEA force control based on model-based and model-free force predictive control methods. The control software architecture is also introduced. The index exoskeleton finger is used as an example for illustration purposes, while keeping in mind that the other exoskeleton fingers use the same method but different values of parameters.

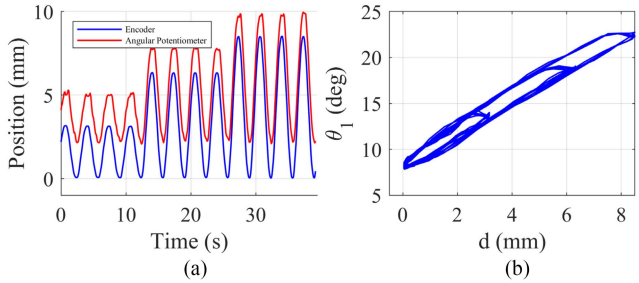

Fig. 8. Backlash illustration. (a) Motor position calculated by encoder and angular potentiometer separately. (b) Relationship between the motor position d and the MCP joint angle θ_1.

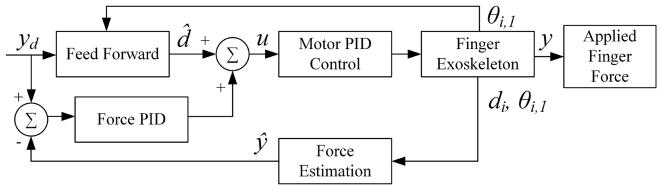

Fig. 9. Force control scheme for a single exoskeleton finger. $\theta_{i,1}$ represents the MCP joints of exoskeleton finger $i (i \in \{1, 2, 3, 4, 5\})$. d_i represents the current motor position of exoskeleton finger i.

A. Backlash Estimation

In order to achieve accurate force control, an elaborate mathematical model needs to be developed. However, the backlash causes a significant effect on the LSEA's force measurement performance. It can be sourced from the backdrivable motor and the linear motion transmission between different parts. Sleeve bearings are used instead of linear bearing due to the limited space, which cannot prevent the backlash during the motion transmission process.

To illustrate and quantify the backlash effects, the index LSEA was excited with a sinusoidal signal to push and pull the output shaft without load. The amplitudes (3, 6, and 8 mm) are changed as time elapses. It was shown in Section II that the force measurement is mainly based on measuring the displacement of the wave disk spring, which is calculated by the readings from the encoder and angular potentiometer. Fig. 8 shows the backlash effect between these two sensors. The gap represents the backlash.

To solve this problem, a mathematical model inspired by [44], [45], and [46] was built to represent the backlash with the assumption that the LSEAs follow a quasi-static condition. It is also worth mentioning that in this article, the leadscrew nut displacement d represents the motor position since the leadscrew is connected to the motor output shaft rigidly and can be calculated by the expression $d = \frac{l\Delta\text{ticks}}{N_{\text{cpr}}} i$. If there is no backlash, the motor position should match the angle of the MCP joint as shown in the following equation:

$$d(t_i) = h(\tan(\theta_1(t_i)) - \tan(\theta_{\text{init}})). \tag{14}$$

Considering the backlash, the angle of the MCP joint can be modeled as shown in the following equation:

$$\theta_1(t_i) = \begin{cases} \tan^{-1}\left[\frac{\alpha(d(t_i)-p_{\text{push}})}{h} + \tan(\theta_{\text{init}})\right], & \dot{d}(t_i) > 0 \\ \tan^{-1}\left[\frac{\alpha(d(t_i)-p_{\text{pull}})}{h} + \tan(\theta_{\text{init}})\right], & \dot{d}(t_i) < 0 \\ \theta_1(t_{i-1}), & \text{otherwise} \end{cases} \tag{15}$$

where $\theta_1(t_i)$ represents the MCP joint angle at time t_i, $d(t_i)$ represents the motor position at time t_i calculated by encoder reading, θ_{init} represents the initial angle of the MCP joint, h represents the height from the LSEA output shaft to the MCP joint, α represents the slope of the linear function, and p_{push} and p_{pull} represent the offsets of push and pull movements. α, p_{push}, and p_{pull} can be calculated from the data collected under no-load conditions.

The inversion of conditional equation (15) can be used to determine the current motor position $d(t_i)$ with respect to the current MCP joint configuration, on condition of backlash. When the load is applied on the fingertip, any further motor movement $\delta d = d_c - d(t_i)$ can be considered as motion without backlash, where d_c is the motor current position under load. The compensation is implemented by substituting $d = \frac{l\Delta\text{ticks}}{N_{\text{cpr}}} i$ into (12) and replacing d with δd. However, when the LSEA changes the direction of motion, the actual movement is continuous, but the derived model is discontinuous. A smooth parameter $\gamma = \frac{1}{1+e^{-\beta \dot{d}(t_i)}}$ based on the sigmoid function is used to eliminate discontinuity. Here, β represents the smoothness between each condition. Thus, the inverse backlash model with a smooth parameter can be expressed as follows:

$$d(t_i) = \frac{h(\tan(\theta_1(t_i)) - \tan(\theta_{\text{init}}))}{\alpha} + p_{\text{push}}\gamma + p_{\text{pull}}(1-\gamma). \tag{16}$$

B. Model-Based Force Control

The goal of the currently designed controller is to track the desired forces applied to the fingertips by the exoskeleton. Fig. 9 shows the proposed control scheme. It is worth mentioning that the action/contact force on the load is assumed to be perpendicular to the last link, for a stable grasp. The estimated action force $\hat{\mathbf{y}}$ magnitude can be expressed as the function $\hat{y} = f(d, \theta_1)$ with respect to the motor current position d and the MCP joint current angle θ_1. Similarly, giving the information of desired action force y_d and measured MCP joint angle θ_1, the required motor position $\hat{d}$, which is predicted by feed-forward part, can be expressed as $\hat{d} = g(y_d, \theta_1)$.

The PID controller with the corresponding feed-forward and feed-back terms is then given by

$$\begin{aligned} \hat{y} &= f(d, \theta_1) \\ e &= y_d - \hat{y} \\ \hat{d} &= g(y_d, \theta_1) \\ u &= \hat{d} + k_p e + k_d \dot{e} + k_i \int e dt. \end{aligned} \tag{17}$$

Considering the kinematics model derived in Section II, $\hat{\mathbf{y}}$ can be estimated by the principle of virtual work, as expressed in

$$\langle \mathbf{T}, \delta\boldsymbol{\theta}_1 \rangle = \langle \hat{\mathbf{y}}, \delta\mathbf{p} \rangle \tag{18}$$

where $\mathbf{T} = \mathbf{F}_{\text{SEA}} \cdot h$, $\mathbf{F}_{\text{SEA}}$ is calculated by solving (12) and (16) simultaneously to take backlash estimation into account, h is the distance from the LSEA output shaft to MCP joint (Fig. 2), $\mathbf{p}$ is the position of endpoints, and $\langle , \rangle$ is the dot product of the vectors. Considering (6), $\hat{\mathbf{y}}$ can be expressed as follows:

$$\hat{\mathbf{y}} = \begin{bmatrix} \hat{y}_x \\ \hat{y}_y \end{bmatrix} = T \cdot \begin{bmatrix} \frac{\tan\theta_3}{J_1 \tan\theta_3 + J_2} \\ \frac{1}{J_1 \tan\theta_3 + J_2} \end{bmatrix} \tag{19}$$

where J_1 is the first element of the Jacobian, J_2 is the second element of the Jacobian, θ_3 is the angle between the last link and x-axis (Fig. 2), and $\hat{y}_x$ and $\hat{y}_y$ are the component of forces $\hat{\mathbf{y}}$ in global x direction and y direction, respectively. Similarly, solving the simultaneous equations of (12) and (15), the estimation of motor position $\hat{d}$ can be calculated based on the desired force y_d and the MCP joint current angle θ_1.

The accuracy of the proposed control method depends on the accuracy of the model-based force estimation function $f(d, \theta_1)$ and motor position estimation function $g(y_d, \theta_1)$. The prerequisites for such functions are the assumptions of no friction force, rigid parts, and no backlash inside the LSEA. However, the actual LSEA system does not satisfy these critical conditions. The simplified mathematical model causes a significant impact on the accuracy of force control.

C. Data-Driven Force Control

To solve the problems mentioned above in an effort to achieve more accurate force control, we propose a data-driven method to estimate the action force $\hat{y} = \hat{f}(d, \theta_1)$ on the fingertip, and the required motor position $\hat{d} = \hat{g}(y_d, \theta_1)$ for the desired force generation. The control scheme that was used is shown in Fig. 9.

The proposed method is inspired by the dynamic mode decomposition methods [47], [48], sparsity in dynamical systems [49], [50], and sparse identification of nonlinear dynamics method [51], [52]. Similarly, the method is based on observations that most physical systems have only a few relevant terms that define the dynamics, making the governing equations sparse in a high-dimensional nonlinear function space. The difference is that our method does not estimate the dynamic model but estimates the output directly based on measurable features. In addition, we added one more strict assumption such that all other unmeasurable features depend on measurable features. To collect the data, the actual action force magnitude vector $[\mathbf{y_m}]_{n\times 1}$ of n samples applied on the fingertip is measured by pressing the finger mechanism on a six-axis load cell, while the actual motor position vector $[\mathbf{d_m}]_{n\times 1}$ is calculated directly from a rotary encoder. The estimation was solved by sparse regression methods.

For the force prediction function $\hat{y} = \hat{f}(d, \theta_1)$, the current motor position and the current angle of the MCP joint θ_1 are selected as basic features since they are either measured directly by sensors or the measured parts are precisely aligned with sensors. Because the directly measured features are not enough for data analysis, we constructed an augmented feature set that consists of nonlinear functions of basic features by looking into the dynamic model under the ideal condition and surmising the relevant term. The feature set includes the constant ($[\mathbf{1}]_{n\times 1}$), polynomial ($[\mathbf{P}]_{n\times 2m}$), trigonometric ($[\mathbf{T_{sin}}]_{n\times 2m}$, $[\mathbf{T_{cos}}]_{n\times 2m}$), and combination of polynomial and trigonometric ($[\mathbf{C_{sin}}]_{n\times m^2}$, $[\mathbf{C_{cos}}]_{n\times m^2}$) terms as shown in the following equations:

$$\mathbf{P} = \begin{bmatrix} d_1 & \cdots & d_1^m & \theta_{1,1} & \cdots & \theta_{1,1}^m \\ \vdots & \ddots & \vdots & \vdots & \ddots & \vdots \\ d_n & \cdots & d_n^m & \theta_{1,n} & \cdots & \theta_{1,n}^m \end{bmatrix} \tag{20}$$

$$\mathbf{T_{sin}} = \begin{bmatrix} \sin(d_1) & \cdots & \sin(md_1) & \sin(\theta_{1,1}) & \cdots & \sin(m\theta_{1,1}) \\ \vdots & \ddots & \vdots & \vdots & \ddots & \vdots \\ \sin(d_n) & \cdots & \sin(md_n) & \sin(\theta_{1,n}) & \cdots & \sin(m\theta_{1,n}) \end{bmatrix} \tag{21}$$

$$\mathbf{T_{cos}} = \begin{bmatrix} \cos(d_1) & \cdots & \cos(md_1) & \cos(\theta_{1,1}) & \cdots & \cos(m\theta_{1,1}) \\ \vdots & \ddots & \vdots & \vdots & \ddots & \vdots \\ \cos(d_n) & \cdots & \cos(md_n) & \cos(\theta_{1,n}) & \cdots & \cos(m\theta_{1,n}) \end{bmatrix} \tag{22}$$

$$\mathbf{C_{sin}} = \begin{bmatrix} d_1\sin(\theta_{1,1}) & \cdots & d_1\sin(m\theta_{1,1}) & \cdots & d_1^m\sin(m\theta_{1,1}) \\ \vdots & & \ddots & & \vdots \\ d_n\sin(\theta_{1,n}) & \cdots & d_n\sin(m\theta_{1,n}) & \cdots & d_n^m\sin(m\theta_{1,n}) \end{bmatrix} \tag{23}$$

$$\mathbf{C_{cos}} = \begin{bmatrix} d_1\cos(\theta_{1,1}) & \cdots & d_1\cos(m\theta_{1,1}) & \cdots & d_1^m\cos(m\theta_{1,1}) \\ \vdots & & \ddots & & \vdots \\ d_n\cos(\theta_{1,n}) & \cdots & d_n\cos(m\theta_{1,n}) & \cdots & d_n^m\cos(m\theta_{1,n}) \end{bmatrix} \tag{24}$$

where m specifies the highest polynomial order. Each row represents the feature values corresponding to the specific data sample. It is worth to mention that it is not necessary to add the combination of polynomial and trigonometric terms if the order is high, since the separate terms have considered linearity and nonlinearity of the data. However, such combination terms provide the diversity of the augmented features when the order is low. The feature matrix $[\mathbf{X_y}]_{n\times(2m^2+6m+1)}$ can be represented as follows:

$$\mathbf{X_y} = [\mathbf{1} \quad \mathbf{P} \quad \mathbf{T_{sin}} \quad \mathbf{T_{cos}} \quad \mathbf{C_{sin}} \quad \mathbf{C_{cos}}] \tag{25}$$

and the force estimation $[\hat{\mathbf{y}}]_{n\times 1}$ can be the linear combination of constructed features matrix with proper weights vector

$[\mathbf{b_y}]_{(2\,m^2+6\,m+1)\times 1}$ as shown in the following equation:

$$\hat{\mathbf{y}} = \mathbf{X_y}\mathbf{b_y}. \tag{26}$$

For the motor position prediction function $\hat{d} = \hat{g}(y_d, \theta_1)$, we constructed $[\mathbf{X_d}]_{n\times(2\,m^2+6\,m+1)}$ by using the same feature matrix structure, estimated the weights vector $[\mathbf{b_d}]_{(2\,m^2+6\,m+1)\times 1}$, and replaced the estimated force $\hat{\mathbf{y}}$ with estimated position $[\hat{\mathbf{d}}]_{n\times 1}$ as shown in the following equation:

$$\hat{\mathbf{d}} = \mathbf{X_d}\mathbf{b_d}. \tag{27}$$

Intuitively, the more features we use, the more accurate predictor we can get. However, previous research [51], [52] has shown that some major features are enough to estimate the original functions under a reasonable precision, making it sparse in the space of possible functions. Moreover, the large number of negligible features wastes the computing power and decreases the control frequency. Given the above conditions, the least absolute shrinkage and selection operator (LASSO) is imported to perform the feature selection and regularization for the accuracy prediction, as shown in the following equations:

$$\underset{\mathbf{b_y}}{\operatorname{argmin}} \left(\frac{1}{2n} ||\mathbf{X_y}\mathbf{b_y} - \mathbf{y_m}||_2^2 + \lambda_y ||\mathbf{b_y}||_1 \right) \tag{28}$$

$$\underset{\mathbf{b_d}}{\operatorname{argmin}} \left(\frac{1}{2n} ||\mathbf{X_d}\mathbf{b_d} - \mathbf{d}||_2^2 + \lambda_d ||\mathbf{b_d}||_1 \right) \tag{29}$$

where λ_y and λ_d are the nonnegative regularization parameters.

By calculating the linear combination of the features created by real-time data, with nonzero weights in $\mathbf{b_y}$ and $\mathbf{b_d}$, $\hat{\mathbf{y}}$ and $\hat{\mathbf{d}}$ are predicted. Theoretically, the proposed data-driven method takes backlash, parts deformation, and friction forces into account since such immeasurable variables are hidden behind the relationships between the measurable data.

D. Control Software Architecture

The exoskeleton control software architecture can be divided into a high-level controller, which runs on a mobile device, and a low-level controller, which runs on the onboard Teensy 4.1 microcontroller.

The high-level controller consists of two parts. The first part is the voice data input from a BT microphone, which will be sent to the configurable voice activation and speaker verification human–machine interference (CVASV HMI) [29]. The CVASV HMI supports customized activation keywords and provides voice-based bio-authentication while converting speech to text. The CVASV HMI will be activated by the bio-authenticated voice command gathered from the user. The type of grasps that need to be performed will be passed to the slip grasp program. The second part is the slip detection program. If the object slips while being lifted, the system will add force incrementally to each SEA. The force command will be sent from the computer to the microcontroller. The two high-level controllers mentioned above run on a computer in parallel to ensure voice commands can be received and executed while sending the commands to low-level controllers. The control structure is shown in Fig. 10.

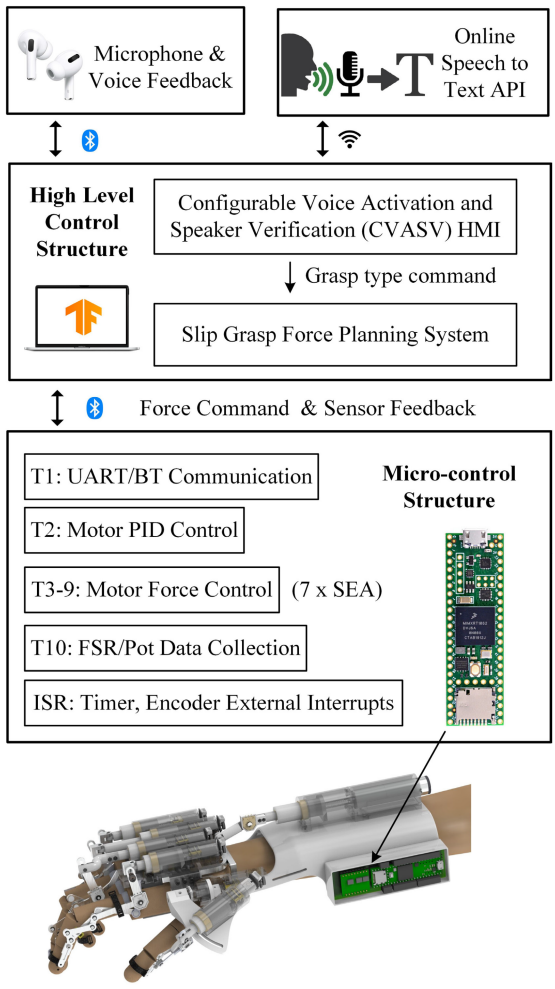

Fig. 10. Illustration of the control software architecture.

The force control process of the LSEAs can be divided into three sections. First, the force command is sent to the microcontroller from the computer grasping program through BT. BT communication thread (T1) will parse the command into the desired force output on each fingertip. Second, the motor force controller (T3) will follow the control schema shown in Fig. 9 to predict the motor position u. Third, the motor force controller (T3) commands the motor PID controller (T2) to regulate the SEA input shaft to achieve desired forces on the fingertips. All seven SEAs run in parallel on T3–T9 at 10 Hz on a Teensy 4.1 microcontroller using FreeRTOS to ensure minimal control latency. The control structure is shown in Fig. 10.

V. Experiments

In this section, we compared the performance of the two proposed control methods and provide the experimental results of the complete exoskeleton glove system.

A. Data Preparation

The data collection is performed on two different test platforms (Fig. 11) to measure the force on the fingertips. During the

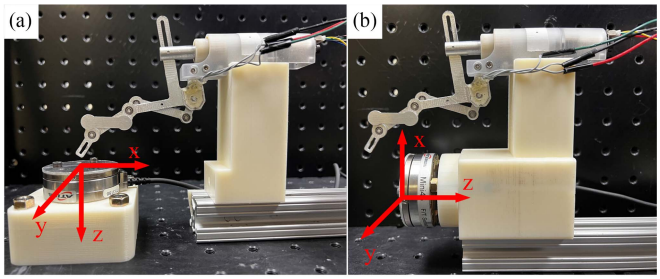

Fig. 11. Test platform with different load cell mounting positions. (a) Load cell is mounted horizontally. (b) load cell is mounted vertically.

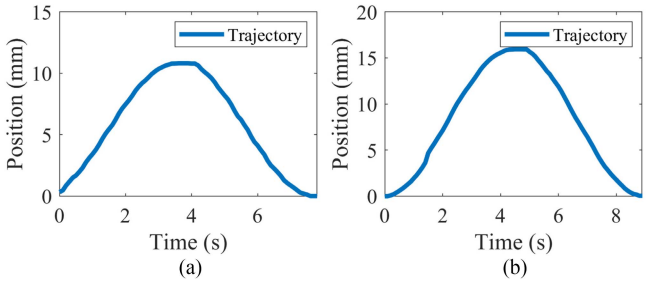

Fig. 12. (a) LSEA motor position trajectory with load cell horizontal installation ($\theta_1 = 12°$). (b) LSEA motor position trajectory with load cell vertical installation ($\theta_1 = 25°$).

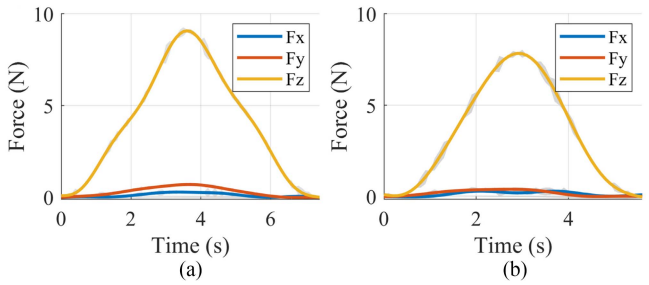

Fig. 13. (a) Force measurement with load cell horizontal installation ($\theta_1 = 12°$). (b) Force measurement with load cell vertical installation ($\theta_1 = 25°$).

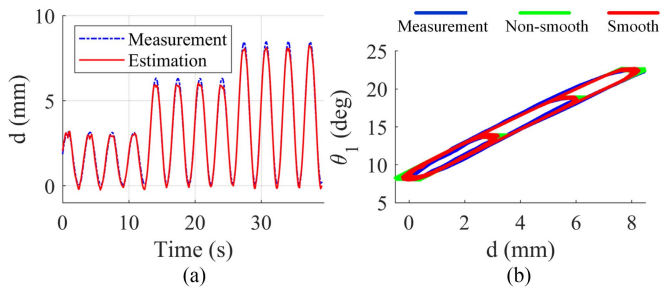

Fig. 14. (a) Comparison between the estimation of motor current position and measurement from encoder. (b) Comparison between the estimation of motor current position and measurement from encoder, related to MCP joint angle θ_1.

data collection process, the LSEA was mounted on a stand that simulates the human hand. The six-axis load cell (ATI mini45, resolution 0.25 N) is fixed either horizontally or vertically to accommodate different exoskeleton finger configurations. The index exoskeleton finger is set up as an example to show the performance.

Considering the force leverage between the LSEA and the fingertip, which depends on the angle of the MCP joint (θ_1), a set of θ_1 (roughly around 10°, 12°, 14°, 19°, 23°, 25°, and 27°) when contact happens is predefined as the test configuration. The motor controller is designed to output a sinusoidal position signal on the leadscrew nut (Fig. 12). The highest normal force is limited to a range from 5 to 10 N by changing the magnitude of the sinusoidal signal. Each angle configuration was performed three times and two of them were randomly selected for training. The remaining data were used for testing. Since the lateral and friction forces are negligible compared with the normal force detected by the load cell as shown in Fig. 13, we assumed that the normal force detected by the load cell is the total reaction force on the fingertip.

B. Fingertip Force Prediction

The backlash model experiments include three identical sets. Each of them repeats a back and forth motion to one of the designed motor positions (3, 6, and 8 mm and initial at 0 mm) four times, continuously. Fig. 14 shows the backlash estimation result based on the defined mathematical model. The root mean squared error for the motor current position estimation based on the current MCP joint angle is 0.27 mm.

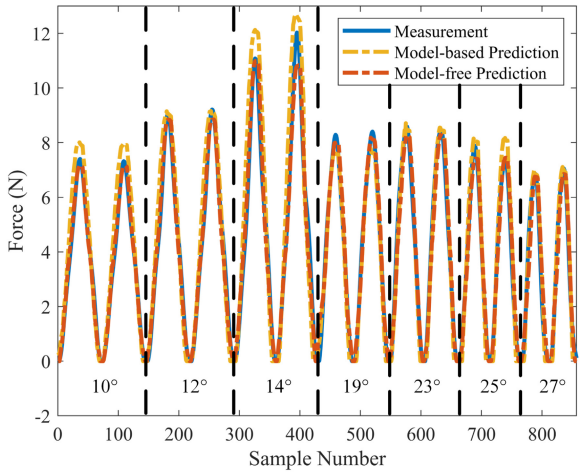

Fig. 15. Force prediction results on training dataset with different θ_1 configurations. Each configuration is performed twice in sequential order. Different configurations are not time related.

The model-based force prediction is implemented with the developed backlash model (Section IV). The results on the training and test datasets are shown in Figs. 15 and 16, respectively. The mean squared errors (mse) on the training dataset and test dataset are 2.65 and 1.46, respectively. In most cases, the model-based calculation is larger than the measurements since the impact of deformable parts and friction force are hard to measure and are not considered in the model. Moreover, the model is not robust enough to counter the vibration noise of the angular potentiometer at the beginning and end of contact. In addition, the backlash

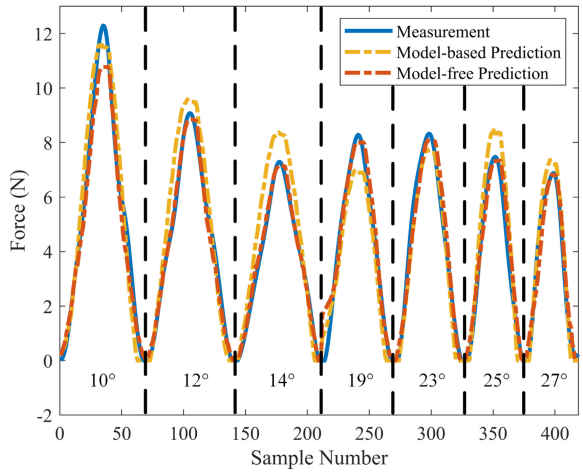

Fig. 16. Force prediction results on test dataset with different θ_1 configurations. Each configuration is performed once. Different configurations are not time related.

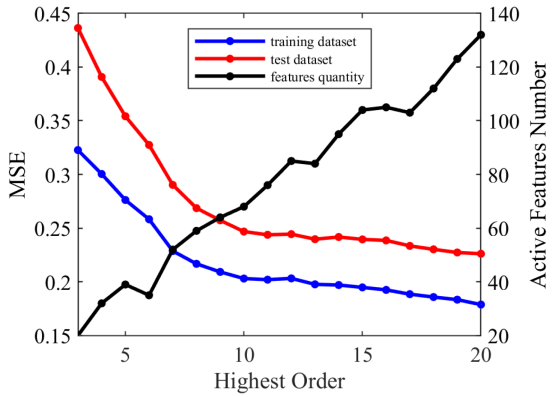

Fig. 17. Comparison of mse on training dataset and test dataset, and active feature numbers with different highest polynomial order.

model is estimated under no-load conditions, which is different compared to the working conditions. Every measurement error or estimation error is accumulated in the final results.

For the model-free force prediction, we compare the mse and the number of active features of the highest polynomial order from 3 to 20 as shown in Fig. 17. The highest polynomial order that equals 10 was picked since the mse decrease slows down while achieving the acceptable active features number. We calculated 100 eligible nonnegative λ_y values and ranked them in an ascending order. The first 50 λ_y were selected to be analyzed. According to the results shown in Fig. 18, as lambda increased, the number of active features dramatically decreases, but the mse increases quickly. Considering the resolution of the load cell, we choose $\lambda_y = 0.0003$, which results in 65 active features in total and achieve acceptable mse (0.20 on the training dataset and 0.25 on the test dataset). The estimation results of the training dataset and the test dataset are shown in Figs. 15 and 16, respectively. It is worth mentioning that the applied fingertip force that is larger than 10 N may not be estimated accurately with low θ_1 configuration since the force exceeds the measuring range of

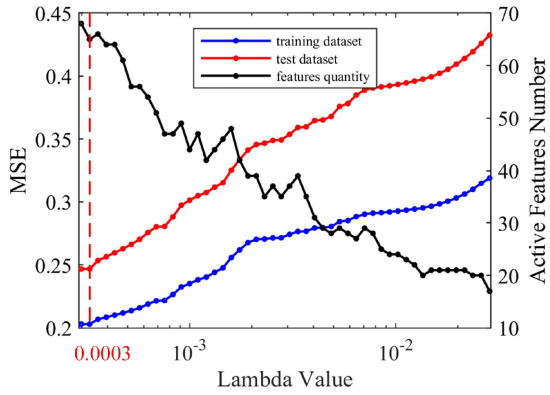

Fig. 18. Comparison of mse on training dataset and test dataset, and active feature numbers with different λ_y value.

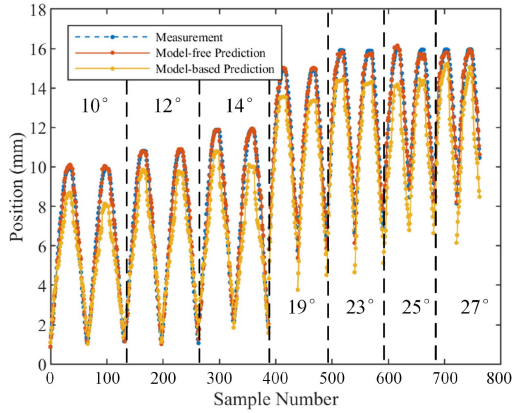

Fig. 19. Results on training dataset with different θ_1 configurations.

the LSEA due to the large mechanical advantage. Besides the advantage of accuracy compared with the model-based method, the model-free force prediction is more robust to vibrational noise at the beginning of the contact and the end of the contact.

Based on the results presented above, the model-free force prediction performs much better than the model-based force prediction.

C. Motor Position Prediction

The motor position prediction is incorporated as the feedforward part in the control system. Since the forces corresponding to the condition where $y_d > 0$ are needed, the part of the data where the measured forces result in $y_m \leq 0$ in the prepared dataset is ignored. The model-based motor position prediction is implemented with the developed backlash model without smoothing since the gradient of the motor position is unknown. Figs. 19 and 20 show the results on the training and the test dataset with different θ_1 configurations. The mse on each dataset are 1.2 and 1.6, respectively. The error mostly occurs when the motor direction is changed, which may be caused by the error of the nonsmooth backlash model as shown in Fig. 14.

For the model-free motor position prediction, we compare the mse and the number of active features of the highest polynomial

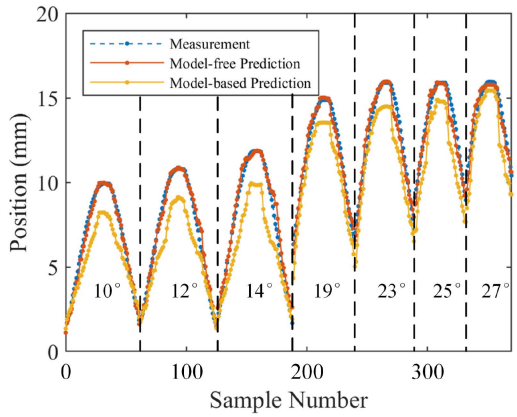

Fig. 20. Results on test dataset with different θ_1 configurations.

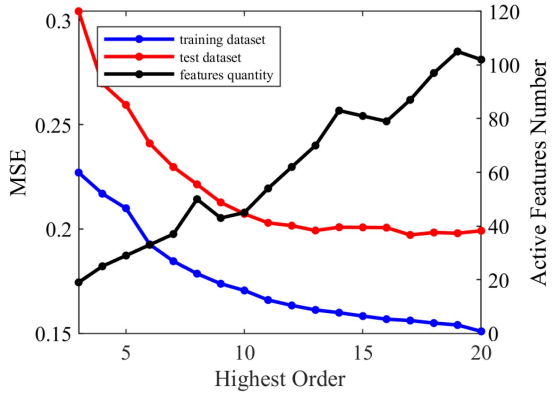

Fig. 21. Results of motor position prediction on training dataset with different θ_1 configurations. Each configuration has two sets of data. The x-axis represents the sample number which is put in time order. Different sets of data are not time related.

order from 3 to 20 as shown in Fig. 21. The highest polynomial of order 13 was selected since the mse decrease slows down and the active features number is acceptable. We calculated 100 eligible nonnegative λ_d and ranked them in ascending order. The first 50 λ_d were selected to be analyzed (Fig. 22). Here, we choose the first one ($\lambda_d = 0.00036$), which results in the lowest mse since the resolution of the encoder is much lower than the calculated mse (0.16 on the training dataset and 0.2 on the test dataset) with an acceptable number of active features. The estimation results of the training dataset and the test dataset are shown in Figs. 19 and 20, respectively. The prediction performs good tracking of the measurement.

Based on the results presented above, the model-free motor position prediction performs much better than the model-based motor position prediction.

D. Control Algorithms Evaluation

The proposed control system should perform and track the desired force applied on the fingertip. Based on the comparison results of the model-based and model-free predictions, the model-free method was selected to be integrated into the final control system. The experiments were performed on the same test platforms as shown in Fig. 11. The readings from the load cell were treated as reference for evaluation. For each mounting position, the exoskeleton finger is required to generate static forces every Newton from 5 to 8 N. According to the results shown in Fig. 23, even with the prediction error and the measurement error, the proposed control algorithms manage to have a stable performance. The mse was 0.42 for the entire experiment.

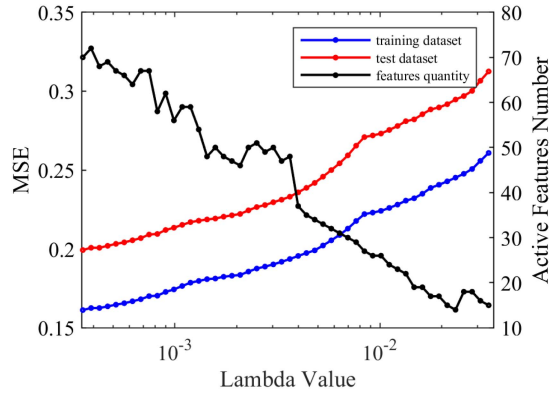

Fig. 22. Results of motor position prediction on test dataset with different θ_1 configurations. Each configuration has one set of data. The x-axis represents the sample number which is put in time order. Different sets of data are not time related.

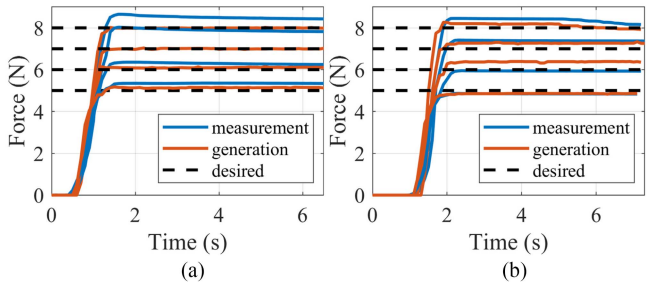

Fig. 23. Comparison between desired force, measured force, and generated force. (a) Experimental results on horizontal platform ($\theta_1 = 14.9°$). (b) Experimental results on vertical platform ($\theta_1 = 21°$).

E. Exoskeleton Glove Grasping Experiments

The goal of the experiments is to evaluate the performance of the whole glove system. The proposed exoskeleton glove system was developed for patients who suffer from brachial plexus injuries whose elbow and shoulder are functional but require assistance to restore the function of the hand for ADLs. Previous research on hand taxonomy shows that there are 33 human grasp types [53]. The five most used grasp types in ADLs are selected for the experiments, which include cylinder grasp, sphere grasp, tip grasp, tripod grasp, and lateral grasp. We selected ten objects that belong to different grasp types for the experiments as shown in Table II.

Because the model-free force prediction and compression prediction are trained based on the load cell measurements that

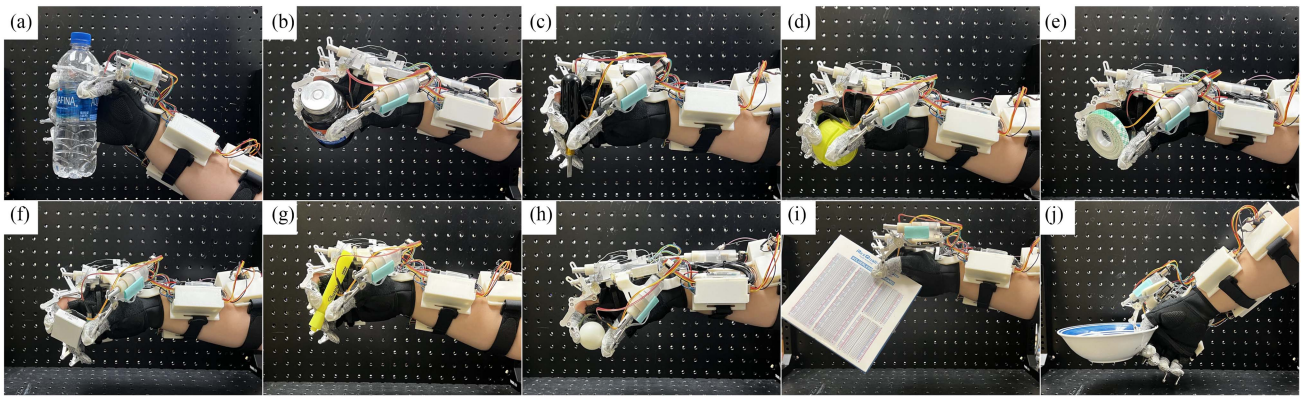

Fig. 24. Examples of successful grasps of each object. Each object is grasped five times by a single participant. (a) Bottle. (b) Jar. (c) Screw driver. (d) Ball. (e) Tape. (f) Small box. (g) Pen. (h) Small ball. (i) Flat box. (j) Bowl.

TABLE II
GOAL OBJECT SELECTION

Name	Grasp type	Weight (g)
Bottle	Cylinder	400
Jar	Cylinder	209
Tape	Tip	15
Small box	Tip	5
Small ball	Tip	5
Screw driver	Tripod	48
Pen	Tripod	15
Flat box	Lateral	142
Bowl	Lateral	316
Ball	Sphere	316

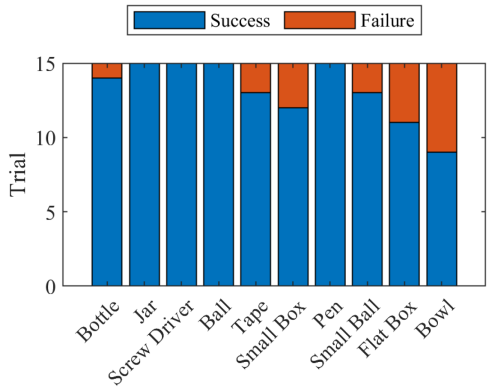

Fig. 25. Experiment results for each objects. The flat box and bowl is hard to grasp since the lateral grasp is hard to be performed with insufficient DOF of thumb linkage.

generate the desired action force $\mathbf{y_d}$ that is normal to the contact surface, the actual desired force $\mathbf{F_d}$, which is perpendicular to the last link based on the assumption, should be converted to $\mathbf{y_d}$ as the input of the control system. Considering that the critical conversion point between two kinds of test platforms is $\theta_1 = 15.2^\circ$ and (19), the magnitude of $\mathbf{y_d}$ is expressed as follows:

$$y_d = \begin{cases} \frac{F_d J_1 \sin\theta_3}{J_2} + F_d \cos\theta_3, & \theta_1 < 15.2^\circ \\ \frac{F_d J_2 \cos\theta_3}{J_1} + F_d \sin\theta_3, & \theta_1 \geq 15.2^\circ \end{cases} \tag{30}$$

where θ_3 is the angle between the last link and the x-axis, and J_1 and J_2 are the components of the Jacobian. The similar conversion equations are applied to the other exoskeleton finger linkages. The force control is activated only if the contact is detected by the FSR sensors on the fingertips.

Three healthy subjects participated in the experiments. The experimental procedure involving human subjects in this article was approved by the Carilion Clinic Institutional Review Board (IRB-19-330). Each of the subjects wore the exoskeleton glove and performed the grasps without any intentional finger movements. The wrist was adjusted to the best grasp position for each subject. Each object was grasped for five times by each participant. For each trial, the exoskeleton glove was activated by voice activation from the participant using the keywords "Hey, glove." After receiving the feedback "activated" from the earphone, the participant should indicate the grasp type (as shown in Table II) based on the goal object through voice command. After receiving another feedback "start" from the earphone, the exoskeleton glove performs the grasp based on the specific grasp type. The initial grasp force on each fingertip was set to be 3 N and the force will be gradually increased by 1 N increments if slipping of the grasped object is detected. The participants were also asked to hold the object up and shake it to show a stable grasp. When the grasp is finished, the participant should give the command "release" to let the glove return to the initial position. It is worth mentioning that the participants should adjust their elbow and shoulder position as needed to help with the grasp.

Fig. 24 shows examples of successful grasps with 10 different objects. Fig. 25 shows the statistical results of 150 trials. The proposed exoskeleton glove system achieves a 100% success rate to grasp a jar, screwdriver, pen, and ball since they belong to the types of grasp that can be easily performed by designing a single DOF trajectory. There were three occasions when the bottle slipped away from the exoskeleton glove due to its smooth surface. For small objects such as a small box, tape, and a small ball, the workspace of the SEA becomes the limitation. The lateral grasp (flat box and bowl) was hard to be performed because of the insufficient DOFs for the thumb motion even with adjustable thumb linkage position. The above results prove that our proposed exoskeleton glove system is able to help with the grasp of daily used objects.

TABLE III
SUMMARY OF HAND EXOSKELETON GRASP ASSISTANCE SYSTEMS

Device	Actuation, transmission	Weight: glove/total	Peak fingertip force	Fingers	Wrist	Force/torque sensing	Intelligent activation
Ryu et al. [54]	Hydraulics, cable	2.62 kg / 2.74 kg	12 N	3	No	Yes	Yes
Nycz et al. [55]	Linear motor, cable	113 g / 867 g	8.7 N	4	No	No	No
Gloreha Lite [56]	Motor, cable	80 g / 5 kg	5 N	5	No	No	No
Hand of Hope [57]	Linear motor, linkage	700 g / –	12 N	5	No	No	No
Dragusanu et al. [58]	Linear motor, linkage	– / around 500 g	–	5	Yes	Yes	No
Ferguson et al. [59]	Motor, cable	– / –	–	3	No	No	No
Graspy Glove [60]	Motor, cable	250 g / 340 g	16 N	4	No	No	No
Agarwal et al. [61]	SEA, cable	80 g / –	–	1	No	Yes	No
KULEX Hand [42]	Motor, linkage	– / 172 g	10 N	2	No	No	No
Our Glove System	**SEA, linkage**	**383 g/759 g**	**10 N**	**5**	**Yes**	**Yes**	**Yes**

F. Comparison With Existing Exoskeleton Glove Systems for Rehabilitation

To better evaluate our proposed system, we compared our exoskeleton glove with eight other devices as shown in Table III. It is worth mentioning that the measurements of peak fingertip force vary from device to device. We used their posted maximum pinch force or measured fingertip force to compare. For most of the devices, the glove on its own is relatively lightweight, but each of them needs a large and heavy actuation system or workstation. Only a few devices cover all five fingers. In addition, none of the other devices considers the impact of wrist movement on grasping. The devices without force/torque sensing can only be implemented with position-based control, which is less effective for rehabilitation [24], [62]. Only the first workstation and our glove system contains an intelligent activation. In comparison, our glove system maintains a stable linkage driven structure while keeping the overall weight in the middle of the eight compared devices. The glove can actuate all five fingers simultaneously and is also capable of providing coupled wrist motion to assist with grasping. The SEAs with force-based control provide the ability to grasp different objects with proper force, which can be used for the latter stages of physical therapy or intelligent control. The integration of a personalized voice activation function increases the convenience of daily use for patients.

VI. CONCLUSION

This article presented the design optimization, control, and development of an exoskeleton glove system for the rehabilitation of patients who suffer from brachial plexus injuries. Each single DOF exoskeleton finger linkage was optimized to imitate human grasp motion. The linear SEAs integrated into the linkage provide the ability to generate and measure contact forces, which enables force control. Two types of force prediction and motor position prediction algorithms, model-based and model-free, were investigated and compared. A mathematical model for the backlash was developed and implemented with model-based prediction. The feature augmentation, feature matrix construction, and feature selection by LASSO regression for model-free prediction were also introduced. The experimental results showed that the proposed model-free prediction methods provide significant improvements. The static force experiments showed that the proposed control system with model-free prediction is able to accomplish accurate force control.

In addition to the exploration of the algorithms, a complete prototype of the proposed exoskeleton glove system was designed and integrated with a total weight of 759 g. To analyze the performance of the exoskeleton glove system, grasping experiments were conducted with three subjects and ten daily used objects that cover five kinds of grasp types. The results with high success rates showed that our exoskeleton glove system has the ability to complete grasping tasks for ADLs.

There are still several aspects of our glove system that could be improved upon. The reduced DOFs of the exoskeleton finger linkages limit the workspace and capability of the glove. This limitation causes difficulties in performing lateral grasps compared with other types of grasps.

Based on our current research, we believe that the proposed exoskeleton glove system is innovative and comfortable to wear due to its combination of portability and dexterity, enabled by novel actuation and control methodologies developed by our team. The intelligent control of the glove system based on the perception of contact forces and hand posture will be implemented.

ACKNOWLEDGMENT

This material is partly based upon work supported by (while serving at) the National Science Foundation.

REFERENCES

[1] M. W. Brault, *Americans With Disabilities: 2010*. Washington, DC: US Department of Commerce Economics and Statistics Administration, 2012.
[2] R. Midha, "Epidemiology of brachial plexus injuries in a multitrauma population," *Neurosurgery*, vol. 40, pp. 1182–1189, 1997.
[3] H. R. Park, G. S. Lee, I. S. Kim, and J.-C. Chang, "Brachial plexus injury in adults," *Nerve*, vol. 3, no. 1, pp. 1–11, 2017.
[4] J. L. Giuffre, S. Kakar, A. T. Bishop, R. J. Spinner, and A. Y. Shin, "Current concepts of the treatment of adult brachial plexus injuries," *J. Hand Surg.*, vol. 35, no. 4, pp. 678–688, 2010.
[5] R. A. Bos et al., "A structured overview of trends and technologies used in dynamic hand orthoses," *J. NeuroEngineering Rehabil.*, vol. 13, no. 1, pp. 1–25, 2016.
[6] A. Borboni, M. Mor, and R. Faglia, "Gloreha-hand robotic rehabilitation: Design, mechanical model, and experiments," *J. Dyn. Syst., Meas. Control*, vol. 138, no. 11, 2016, Art. no. 111003.
[7] F. Orihuela-Espina et al., "Robot training for hand motor recovery in subacute stroke patients: A randomized controlled trial," *J. Hand Ther.*, vol. 29, no. 1, pp. 51–57, 2016.
[8] J. Iqbal, N. Tsagarakis, A. E. Fiorilla, and D. Caldwell, "Design requirements of a hand exoskeleton robotic device," in *Proc. 14th IASTED Int. Conf. Robot. Appl.*, 2009, vol. 664, no. 81, pp. 44–51.
[9] P. Polygerinos, Z. Wang, K. C. Galloway, R. J. Wood, and C. J. Walsh, "Soft robotic glove for combined assistance and at-home rehabilitation," *Robot. Auton. Syst.*, vol. 73, pp. 135–143, 2015.
[10] S. Kudo, K. Oshima, M. Arizono, Y. Hayashi, and S. Moromugi, "Electric-powered glove for CCI patients to extend their upper-extremity function," in *Proc. IEEE/SICE Int. Symp. Syst. Integration*, 2014, pp. 638–643.

[11] R. Deimel and O. Brock, "A novel type of compliant and underactuated robotic hand for dexterous grasping," *Int. J. Robot. Res.*, vol. 35, no. 1-3, pp. 161–185, 2016.

[12] F. Ilievski, A. D. Mazzeo, R. F. Shepherd, X. Chen, and G. M. Whitesides, "Soft robotics for chemists," *Angewandte Chemie*, vol. 123, no. 8, pp. 1930–1935, 2011.

[13] H. K. Yap, B. W. Ang, J. H. Lim, J. C. Goh, and C. H. Yeow, "A fabric-regulated soft robotic glove with user intent detection using EMG and RFID for hand assistive application," in *Proc. IEEE Int. Conf. Robot. Automat.*, 2016, vol. 2016, pp. 3537–3542.

[14] Z. Ma, P. Ben-Tzvi, and J. Danoff, "Sensing and force-feedback exoskeleton robotic (SAFER) glove mechanism for hand rehabilitation," in *Proc. ASME Des. Eng. Tech. Conf.*, 2015, vol. 5A, pp. 1–8.

[15] M. Aiple and A. Schiele, "Pushing the limits of the CyberGrasp for haptic rendering," in *Proc. IEEE Int. Conf. Robot. Automat.*, 2013, pp. 3541–3546.

[16] U. A. Hofmann, T. Bützer, O. Lambercy, and R. Gassert, "Design and evaluation of a Bowden-cable-based remote actuation system for wearable robotics," *IEEE Robot. Automat. Lett.*, vol. 3, no. 3, pp. 2101–2108, Jul. 2018.

[17] D. Leonardis et al., "An EMG-controlled robotic hand exoskeleton for bilateral rehabilitation," *IEEE Trans. Haptics*, vol. 8, no. 2, pp. 140–151, Apr./Jun. 2015.

[18] N. S. K. Ho et al., "An EMG-driven exoskeleton hand robotic training device on chronic stroke subjects: Task training system for stroke rehabilitation," in *Proc. IEEE Int. Conf. Rehabil. Robot.*, 2011, pp. 1–5.

[19] I. Sarakoglou, A. Brygo, D. Mazzanti, N. G. Hernandez, D. G. Caldwell, and N. G. Tsagarakis, "Hexotrac: A highly under-actuated hand exoskeleton for finger tracking and force feedback," in *Proc. IEEE/RSJ Int. Conf. Intell. Robots Syst.*, 2016, pp. 1033–1040.

[20] M. Malvezzi, T. L. Baldi, A. Villani, F. Ciccarese, and D. Prattichizzo, "Design, development, and preliminary evaluation of a highly wearable exoskeleton," in *Proc. 29th IEEE Int. Conf. Robot Hum. Interactive Commun.*, 2020, pp. 1055–1062.

[21] A. Chiri, N. Vitiello, F. Giovacchini, S. Roccella, F. Vecchi, and M. C. Carrozza, "Mechatronic design and characterization of the index finger module of a hand exoskeleton for post-stroke rehabilitation," *IEEE/ASME Trans. Mechatronics*, vol. 17, no. 5, pp. 884–894, Oct. 2012.

[22] A. A. Blank, J. A. French, A. U. Pehlivan, and M. K. O'Malley, "Current trends in robot-assisted upper-limb stroke rehabilitation: Promoting patient engagement in therapy," *Curr. Phys. Med. Rehabil. Rep.*, vol. 2, no. 3, pp. 184–195, 2014.

[23] R. Colombo et al., "Robotic techniques for upper limb evaluation and rehabilitation of stroke patients," *IEEE Trans. Neural Syst. Rehabil. Eng.*, vol. 13, no. 3, pp. 311–324, Sep. 2005.

[24] A. U. Pehlivan, F. Sergi, and M. K. O'Malley, "A subject-adaptive controller for wrist robotic rehabilitation," *IEEE/ASME Trans. Mechatronics*, vol. 20, no. 3, pp. 1338–1350, Jun. 2015.

[25] W. S. Harwin, T. Rahman, and R. A. Foulds, "A review of design issues in rehabilitation robotics with reference to North American research," *IEEE Trans. Rehabil. Eng.*, vol. 3, no. 1, pp. 3–13, Mar. 1995.

[26] E. M. Refour, B. Sebastian, R. J. Chauhan, and P. Ben-Tzvi, "A general purpose robotic hand exoskeleton with series elastic actuation," *J. Mechanisms Robot.*, vol. 11, no. 6, 2019, Art. no. 060902.

[27] T. Vanteddu, B. Sebastian, and P. Ben-Tzvi, "Design optimization of RML glove for improved grasp performance," in *Proc. ASME Dyn. Syst. Control Conf.*, American Society of Mechanical Engineers, 2018, vol. 51890, Art. no. V001T07A004.

[28] J. Lee and P. Ben-Tzvi, "Design of a wearable 3-DOF forearm exoskeleton for rehabilitation and assistive purposes," in *Proc. ASME Int. Mech. Eng. Congr. Expo.,* 2017, vol. 3, pp. 1–10.

[29] Y. Guo, W. Xu, S. Pradhan, C. Bravo, and P. Ben-Tzvi, "Integrated and configurable voice activation and speaker verification system for a robotic exoskeleton glove," in *Proc. Int. Des. Eng. Tech. Conf. Comput. Inf. Eng. Conf.*, American Society of Mechanical Engineers, 2020, vol. 83990, Art. no. V010T10A043.

[30] Y. Guo, W. Xu, S. Pradhan, C. Bravo, and P. Ben-Tzvi, "Personalized voice activated grasping system for a robotic exoskeleton glove," *Mechatronics*, vol. 83, 2022, Art. no. 102745.

[31] E. Refour, B. Sebastian, and P. Ben-Tzvi, "Design and integration of a two-digit exoskeleton glove," in *Proc. ASME Des. Eng. Tech. Conf.*, 2017, vol. 5A, pp. 1–8.

[32] A. J. Kurdila and P. Ben-Tzvi, *Dynamics and Control of Robotic Systems*. Hoboken, NJ, USA: Wiley, 2019.

[33] J. F. Soechting and M. Flanders, "Flexibility and repeatability of finger movements during typing: Analysis of multiple degrees of freedom," *J. Comput. Neurosci.*, vol. 4, no. 1, pp. 29–46, 1997.

[34] G. A. Bekey, R. Tomovic, and I. Zeljkovic, "Control architecture for the Belgrade/USC hand," in *Dextrous Robot Hands*. New York, NY, USA: Springer, 1990, pp. 136–149.

[35] Z. Ma, P. Ben-Tzvi, and J. Danoff, "Hand rehabilitation learning system with an exoskeleton robotic glove," *IEEE Trans. Neural Syst. Rehabil. Eng.*, vol. 24, no. 12, pp. 1323–1332, Dec. 2016.

[36] E. Refour, B. Sebastian, and P. Ben-Tzvi, "Two-digit robotic exoskeleton glove mechanism: Design and integration," *J. Mechanisms Robot.*, vol. 10, no. 2, 2018, Art. no. 025002.

[37] M. Valenzuela and B. Bordoni, *Anatomy, Shoulder and Upper Limb, Hand Dorsal Interossei Muscle*. Treasure Island, FL, USA: StatPearls Publishing, 2020.

[38] B. J. Lee, A. Williams, and P. Ben-Tzvi, "Intelligent object grasping with sensor fusion for rehabilitation and assistive applications," *IEEE Trans. Neural Syst. Rehabil. Eng.*, vol. 26, no. 8, pp. 1556–1565, Aug. 2018.

[39] B. Alexander and K. Viktor, "Proportions of hand segments," *Int. J. Morphol.*, vol. 28, no. 3, pp. 755–758, 2010.

[40] M. Liu, "Hust dataset (March 2016)," Mar. 2016. [Online]. Available: https://www.handcorpus.org/?p=1596

[41] G. Pratt and M. Williamson, "Series elastic actuators," in *Proc. IEEE/RSJ Int. Conf. Intell. Robots Syst. Hum. Robot Interact. Cooperative Robots*, 1995, vol. 1, pp. 399–406.

[42] M. B. Hong, S. J. Kim, Y. S. Ihn, G.-C. Jeong, and K. Kim, "KULEX-hand: An underactuated wearable hand for grasping power assistance," *IEEE Trans. Robot.*, vol. 35, no. 2, pp. 420–432, Apr. 2019.

[43] W. Xu, S. Pradhan, Y. Guo, C. Bravo, and P. Ben-Tzvi, "A novel design of a robotic glove system for patients with brachial plexus injuries," in *Proc. Int. Des. Eng. Tech. Conf. Comput. Inf. Eng. Conf.*, American Society of Mechanical Engineers, 2020, vol. 83990, Art. no. V010T10A042.

[44] Y. Yun, P. Agarwal, J. Fox, K. E. Madden, and A. D. Deshpande, "Accurate torque control of finger joints with UT hand exoskeleton through Bowden cable SEA," in *Proc. IEEE/RSJ Int. Conf. Intell. Robots Syst.*, 2016, pp. 390–397.

[45] V. Agrawal, "Modeling and control of cable actuated surgical robotic systems," Ph.D. dissertation, Purdue University, West Lafayette, IN, USA, 2011.

[46] T. Do, T. Tjahjowidodo, M. Lau, T. Yamamoto, and S. Phee, "Hysteresis modeling and position control of tendon-sheath mechanism in flexible endoscopic systems," *Mechatronics*, vol. 24, no. 1, pp. 12–22, 2014.

[47] C. W. Rowley, I. Mezić, S. Bagheri, P. Schlatter, and D. S. Henningson, "Spectral analysis of nonlinear flows," *J. Fluid Mechanics*, vol. 641, pp. 115–127, 2009.

[48] P. J. Schmid, "Dynamic mode decomposition of numerical and experimental data," *J. Fluid Mechanics*, vol. 656, pp. 5–28, 2010.

[49] H. Schaeffer, R. Caflisch, C. D. Hauck, and S. Osher, "Sparse dynamics for partial differential equations," *Proc. Nat. Acad. Sci. USA*, vol. 110, no. 17, pp. 6634–6639, 2013.

[50] V. Ozoliņš, R. Lai, R. Caflisch, and S. Osher, "Compressed modes for variational problems in mathematics and physics," *Proc. Nat. Acad. Sci. USA*, vol. 110, no. 46, pp. 18368–18373, 2013.

[51] S. L. Brunton, J. L. Proctor, and J. N. Kutz, "Discovering governing equations from data by sparse identification of nonlinear dynamical systems," *Proc. Nat. Acad. Sci. USA*, vol. 113, no. 15, pp. 3932–3937, 2016.

[52] E. Kaiser, J. N. Kutz, and S. L. Brunton, "Sparse identification of nonlinear dynamics for model predictive control in the low-data limit," in *Proc. Roy. Soc. A*, 2018, vol. 474, no. 2219, Art. no. 20180335.

[53] T. Feix, J. Romero, H. B. Schmiedmayer, A. M. Dollar, and D. Kragic, "The GRASP taxonomy of human grasp types," *IEEE Trans. Human-Mach. Syst.*, vol. 46, no. 1, pp. 66–77, Feb. 2016.

[54] D. Ryu et al., "Micro hydraulic system using slim artificial muscles for a wearable haptic glove," in *Proc. IEEE/RSJ Int. Conf. Intell. Robots Syst.*, 2008, pp. 3028–3033.

[55] C. J. Nycz, T. Bützer, O. Lambercy, J. Arata, G. S. Fischer, and R. Gassert, "Design and characterization of a lightweight and fully portable remote actuation system for use with a hand exoskeleton," *IEEE Robot. Automat. Lett.*, vol. 1, no. 2, pp. 976–983, Jul. 2016.

[56] "Gloreha glove," Accessed: Feb. 2, 2022. [Online]. Available: https://www.gloreha.com/maestro/

[57] X. Hu, K. Tong, X. Wei, W. Rong, E. Susanto, and S. Ho, "The effects of post-stroke upper-limb training with an electromyography (EMG)-driven hand robot," *J. Electromyogr. Kinesiol.*, vol. 23, no. 5, pp. 1065–1074, 2013.

[58] M. Dragusanu, M. Z. Iqbal, T. L. Baldi, D. Prattichizzo, and M. Malvezzi, "Design, development, and control of a hand/wrist exoskeleton for rehabilitation and training," *IEEE Trans. Robot.*, vol. 38, no. 3, pp. 1472–1488, Jun. 2022.
[59] P. W. Ferguson, B. Dimapasoc, Y. Shen, and J. Rosen, "Design of a hand exoskeleton for use with upper limb exoskeletons," in *Proc. Int. Symp. Wearable Robot.*, Springer, 2018, pp. 276–280.
[60] D. Popov, I. Gaponov, and J.-H. Ryu, "Portable exoskeleton glove with soft structure for hand assistance in activities of daily living," *IEEE/ASME Trans. Mechatronics*, vol. 22, no. 2, pp. 865–875, Apr. 2017.
[61] P. Agarwal, J. Fox, Y. Yun, M. K. O'Malley, and A. D. Deshpande, "An index finger exoskeleton with series elastic actuation for rehabilitation: Design, control and performance characterization," *Int. J. Robot. Res.*, vol. 34, no. 14, pp. 1747–1772, 2015.
[62] C. Li, Z. Rusák, I. Horváth, L. Ji, and Y. Hou, "Current status of robotic stroke rehabilitation and opportunities for a cyber-physically assisted upper limb stroke rehabilitation," in *Proc. Int. Tools Methods Competitive Eng. Symp.*, 2014, vol. 1, pp. 899–914.

Wenda Xu received the B.S. degree in mechanical engineering from Hunan University, Hunan, China, in 2016 and the M.S. degree in mechanical engineering from Columbia University, New York, NY, USA, in 2019. He is currently working toward the Ph.D. degree in mechanical engineering with Virginia Tech, Blacksburg, VA, USA.

His research interests include robotics design, artificial intelligence, and machine learning.

Yunfei Guo received the B.S. and M.S. degrees in electrical and computer engineering in 2019 and 2020, respectively, from Virginia Tech, Blacksburg, VA, USA, where he is currently working toward the Ph.D. degree in electrical and computer engineering.

His research interests are in machine learning applications in embedded system and ubiquitous computing.

Cesar Bravo received the B.A. degree in applied mathematics and science from King College, Bristol, TN, in 1992, the B.S. degree in biomedical engineering, engineering science, and mechanics from the University of Tennessee at Knoxville, Knoxville, TN, USA, in 1995, and the medical degree (*magna cum laude*) from the University of Puerto Rico School of Medicine, Río Piedras, Puerto Rico, in 1999.

After completing an internship in general surgery and his residency in orthopaedic surgery there, he completed a fellowship in hand surgery at the Mayo Clinic in 2005. Dr. Bravo has specialized in hand and upper extremity surgery with a particular interest in problems of the elbow at Carilion Clinic since 2005. He is certified by the American Board of Orthopaedic Surgery in orthopedics and hand surgery.

Pinhas Ben-Tzvi (Senior Member, IEEE) received the B.S. degree (*summa cum laude*) from the Technion—Israel Institute of Technology, Haifa, Israel, in 2000, and the M.S. and Ph.D. degrees from the University of Toronto, Toronto, ON, Canada, in 2004 and 2008, respectively, all in mechanical engineering.

He is currently a Professor of mechanical engineering and electrical and computer engineering, and the founding Director of the Robotics and Mechatronics Laboratory, Virginia Tech, Blacksburg, VA, USA. His expertise and interests span the areas of cyber–physical systems, machine learning, robotics and intelligent autonomous systems, healthcare technologies, human–machine interactions, multirobot systems, systems dynamics and control, mechatronics design, and novel sensing and actuation. His research program was supported by a wide variety of government agencies, and he has authored and coauthored more than 175 peer-reviewed journal articles and refereed papers in conference proceedings and is the named inventor on 12 U.S. patents and patent applications.

Dr. Ben-Tzvi is the recipient of several teaching, research, and professional service excellence awards, and served on various journal and conference editorial boards as an Editor and Associate Editor. He is a Fellow of the ASME.